Astronomy & Astrophysics manuscript no. aaagb3dfirstgrid
August 26, 2016

Global 3D radiation-hydrodynamics models of AGB stars

Effects of convection and radial pulsations on atmospheric structures

B. Freytag, S. Liljegren, and S. Höfner

Division of Astronomy and Space Physics, Department of Physics and Astronomy, Uppsala University, Box 516, SE-751 20 Uppsala, Sweden (e-mail: Bernd.Freytag@physics.uu.se)

Started 2015-05-29; Received ...; accepted ...

ABSTRACT

Context. Observations of asymptotic giant branch (AGB) stars with increasing spatial resolution reveal new layers of complexity of atmospheric processes on a variety of scales.
Aims. To analyze the physical mechanisms that lie behind asymmetries and surface structures in observed images we use detailed three-dimensional dynamical simulations of AGB stars, which self-consistently describe convection and pulsations.
Methods. We use the CO5BOLD radiation-hydrodynamics code to produce an exploratory grid of global "star-in-a-box" models of the outer convective envelope and the inner atmosphere of AGB stars to study convection, pulsations, and shock waves and their dependence on stellar and numerical parameters.
Results. The model dynamics are governed by the interaction of long-lasting giant convection cells, short-lived surface granules, and strong, radial, fundamental-mode pulsations. Radial pulsations and shorter-wavelength acoustic waves (convective noise) induce shocks on various scales in the atmosphere. Convection, waves, and shocks all contribute to the dynamical pressure – and thus to an increase of the stellar radius and a to levitation of material into layers where dust can form. Consequently, the resulting relation of pulsation period and stellar radius is shifted towards larger radii compared to that of nonlinear one-dimensional models. The dependence of pulsation period on luminosity agrees well with observed relations. The interaction of the pulsation mode with the non-stationary convective flow causes occasional amplitude changes and phase shifts. The regularity of the pulsations decreases with decreasing gravity as the relative size of convection cells increases. The model stars don't have a well-defined surface. Instead, the light is emitted from a very extended inhomogeneous atmosphere with a complex dynamic pattern of high-contrast features.
Conclusions. Our models self-consistently describe convection, convectively-generated acoustic noise, fundamental-mode radial pulsations, and atmospheric shocks of various scales, that give rise to complex changing structures in the atmospheres of AGB stars.

Key words. convection – shock waves – methods: numerical – stars: AGB and post-AGB – stars: atmospheres – stars: oscillations (including pulsations)

1. Introduction

Variability with typical periods of 100 – 1000 days is a characteristic feature of stars on the asymptotic giant branch (AGB). The pronounced changes of the stellar luminosity are generally attributed to low-order large-amplitude pulsations. Various correlations between pulsation properties and stellar parameters have been derived from observations, e.g., period-luminosity (P-L) relations. Evolved AGB stars, Mira variables, follow a linear P-L relationship, similar to that of Cepheids, where a larger luminosity results in a longer period (see e.g. Whitelock et al. 2008, 2009). Less evolved AGB stars, however, fall on a series of parallel P-L sequences, according to Wood et al. (1999). These sequences are interpreted as representing stars pulsating in various modes, with Mira variables pulsating in the fundamental mode while low-amplitude variables pulsate in overtones.

Pulsation and convection seem to play a decisive role for the heavy mass loss experienced by AGB stars. The observed outflows, with typical velocities of 5 – 20 $\mathrm{km\,s^{-1}}$ and mass loss rates in the range of 10^{-8} – $10^{-4}\,\mathrm{M_\odot\,yr^{-1}}$, are – according to the standard picture – accelerated by radiative pressure on dust grains, which are formed at about 2 – 3 stellar radii. Pulsations and non-stationary convective flows trigger strong atmospheric shock waves, which lift gas out to distances where temperatures are low enough and gas densities sufficiently high to allow for the condensation of dust particles (for a recent review on this mass loss scenario, see, e.g., Höfner 2015).

Classically, variable stars have been analyzed via their light curves, which have been obtained for a large sample of objects and are usually regular for evolved AGB stars. However, high-resolution observations of near-by stars reveal complex irregular structures and dynamical phenomena on various spatial and temporal scales.

For example for Mira (o Cet), Karovska et al. (1991) used speckle interferometry with various telescopes to detect asymmetries in the extended atmosphere that changed over time. Later, Karovska et al. (1997) speculated that the asymmetries detected with HST/Foc in the UV and optical might be due to spots or non-radial pulsations. Lopez et al. (1997) found a best fit to observations in the IR taken with ISI by models with inhomogeneities or clumps. Chandler et al. (2007) presented a number of explanations for their ISI observations, among them shock waves and non-uniform dust formation. Recently, Stewart et al. (2016b) produced images of Mira by analyzing occultations by Saturn's rings observed with the Cassini spacecraft showing layers and asymmetries in the stellar atmosphere.

It should however be noted that some phenomena may not be intrinsic to the star itself, since Mira is part of a binary system,

and the complex large-scale structure of the envelope may be attributed to wind-wind interaction (Ramstedt et al. 2014).

However, similar clumpy and non-spherical structures can be found around other AGB stars. For instance, very recently, Ohnaka et al. (2016) observed the semi-regular (type a) star W Hya with VLT/SPHERE-ZIMPOL and VLTI/AMBER and find supporting evidence for clumpy dust clouds caused by by pulsations and large convective cells, as predicted by 3D simulations for AGB stars.

Quite a number of observations exist of the carbon star IRC+10216 (CW Leo), starting with the first detection of a bipolar asymmetry in coronographic images by Kastner & Weintraub (1994). Haniff & Buscher (1998) attribute asymmetries in diffraction-limited interferometric images to envelope clearing along a bipolar axis. Weigelt et al. (1998) used speckle-masking interferometry with the SAO 6m telescope to find an "extremely clumpy" dust shell, that "gives most likely direct evidence for an inhomogeneous mass-loss process which may be interpreted in terms of large-scale surface convection-cells (Schwarzschild 1975) being a common phenomenon for red giants." Recently, Stewart et al. (2016a) demonstrated the dynamical evolution of dust clouds in images reconstructed from aperture-masking interferometric observations using Keck and the VLT and from occultation measurements by Cassini, resulting in a complete change in patterns compared to the earliest data.

The reason for these observed asymmetries could be the underlying irregular global convective flows in AGB stars, although the star itself or the stellar surface are not directly visible.

A realistic modeling of the underlying physical processes is a notoriously difficult problem and theoretical studies found in the literature are usually restricted to one-dimensional (1D) simulations. Still, dynamical 1D atmosphere-&-wind models have been used successfully to explore the basic dust-driven mass-loss process, relying on a parameterized description of sub-photospheric velocities due to radial pulsations (so-called piston models; see, e.g., Bowen 1988; Fleischer et al. 1992; Winters et al. 2000; Höfner et al. 2003; Jeong et al. 2003; Höfner 2008). Mass loss rates and wind velocities, as well as spectral energy distributions, variations of photometric colors with pulsation phase, and other observable properties resulting from the latest generation of such time-dependent atmosphere-&-wind models computed with the DARWIN code show good agreement with observations (Nowotny et al. 2010; Eriksson et al. 2014; Bladh et al. 2015).

One-dimensional CODEC models of gas dynamics in the stellar interior and atmosphere, simulating (radial) Mira-type pulsations as self-excited oscillations and following the propagation of the resulting shock waves through the stellar atmosphere have been presented for instance by Ireland et al. (2008, 2011).

Despite their success in reproducing various observational results, 1D dynamical models are not sufficient to give a comprehensive picture of the physical processes leading to mass loss on the AGB: they require a number of free parameters that have to be carefully adjusted, e.g., to describe the variable inner boundary in piston models or the time-dependent extension of the mixing-length theory (MLT) in non-linear pulsation models. Further, such models cannot simulate intrinsically three-dimensional phenomena like stellar convection and can therefore not describe the giant convection cells that are thought to give rise to the non-spherical and clumpy morphology of the atmosphere.

Turbulent flows, as for instance stellar convection, are known to produce acoustic waves if the Mach number is sufficiently large (Lighthill 1952). This excitation process has been studied with local 3D radiation-hydrodynamics simulations for the case of the Sun, e.g., by Nordlund & Stein (2001) and Stein & Nordlund (2001). The steepening of these waves while travelling upward into the chromosphere was investigated by Wedemeyer et al. (2004). Such local 3D radiation-hydrodynamics simulations have been used for decades to model small patches on the surface of (more or less) solar-type stars. Now a number of grids from different groups and codes are available (Ludwig et al. 2009; Magic et al. 2013; Beeck et al. 2013), which even include the regime of white dwarfs (Tremblay et al. 2015).

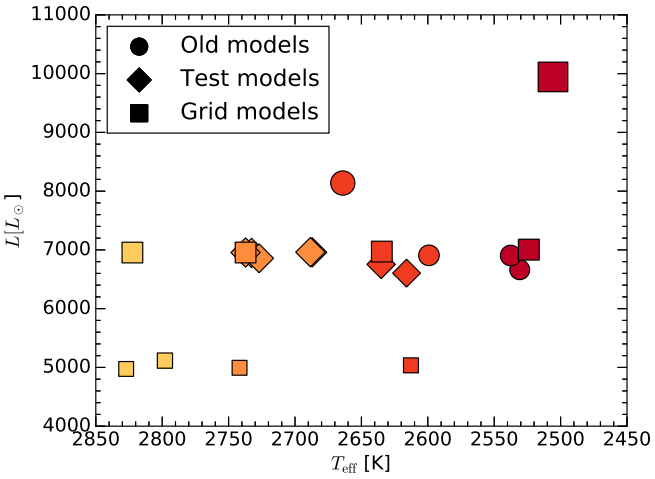

Fig. 1. The luminosity and effective temperature of all models. The colors of the markers represent the temperature of the models while the size of the markers represent the luminosity. The shape of the markers indicates which group in Table 1 the models belong to; the "old" models from (Freytag & Höfner 2008) are circles, the "test" models with varied numerical parameters are diamonds, and the "grid" models with different stellar parameters are squares.

In contrast to these compact types of stars, giants might be covered by only a small number of huge convective cells, as suggested by Stothers & Leung (1971) as an explanation for irregularities in the light curves. Schwarzschild (1975) argued that, if the size of surface convection cells is governed by some characteristic length scale as, for instance, the density scale height, the counterpart of small solar granules should be huge convective structures on giants. Consequently, these stars should produce large-scale acoustic waves. Surface convection and associated waves, pulsation, and shocks have been investigated with global 3D radiation-hydrodynamics simulations with the CO5BOLD code (Freytag et al. 2012), both for the case of red supergiants, for instance by Freytag et al. (2002) and Chiavassa et al. (2009), and with an exploratory study for an AGB star by Freytag & Höfner (2008). These studies confirm the existence of large-scale convection cells and acoustic waves.

In this paper, we present a first grid of AGB-star models, produced with an new, improved version of CO5BOLD. We analyze the dependence of the properties of convection and pulsations on stellar parameters and look at the influence of rotation.

2. Setup of global AGB-star models with CO5BOLD

Following our earlier work (Freytag & Höfner 2008), we present new radiation-hydrodynamics simulations of AGB stars with CO5BOLD (Freytag et al. 2012). Improvements regarding the accuracy and the stability of the hydrodynamics solver are outlined in Freytag (2013).

Table 1. Basic model parameters

model	$M_\star$ $M_\odot$	$M_{\rm env}$ $M_\odot$	$L_\star$ $L_\odot$	$n_x \times n_y \times n_z$	$x_{\rm box}$ $R_\odot$	$P_{\rm rot}$ yr	$t_{\rm avg}$ yr	$R_\star$ $R_\odot$	$T_{\rm eff}$ K	$\log g$ (cgs)	$P_{\rm puls}$ yr	$\sigma_{\rm puls}$ yr
st28gm06n02	1.0	0.196	7079	127^3	1244	∞	11.01	437	2531	-0.85	1.400	0.956
st28gm06n03	1.0	0.188	6589	171^3	1674	∞	2.41	400	2599	-0.77	1.379	0.351
st28gm06n05	1.0	0.187	8144	171^3	1674	∞	2.06	423	2664	-0.82	1.775	1.093
st28gm06n06	1.0	0.186	6905	171^3	1674	∞	4.48	430	2538	-0.83	1.420	0.907
st28gm06n13	1.0	0.181	6932	281^3	1381	∞	29.96	384	2687	-0.73	1.479	0.586
st28gm06n16	1.0	0.178	6582	401^3	1381	∞	23.30	395	2616	-0.76	1.376	0.449
st28gm06n18	1.0	0.182	6781	401^3	1970	∞	26.75	395	2635	-0.76	1.325	0.459
st28gm06n24	1.0	0.182	6944	281^3	1381	∞	23.77	372	2733	-0.71	1.262	0.339
st28gm06n25	1.0	0.182	6890	401^3	1970	∞	23.77	372	2727	-0.71	1.388	0.360
st28gm06n29	1.0	0.182	6956	281^3	1381	20	25.35	384	2688	-0.73	1.297	0.337
st28gm06n30	1.0	0.182	6951	281^3	1381	10	25.34	395	2652	-0.76	1.327	0.200
st28gm07n001	1.0	0.176	10028	281^3	1381	∞	30.90	531	2506	-1.02	2.247	1.397
st26gm07n002	1.0	0.544	6986	281^3	1381	∞	25.35	437	2524	-0.85	1.625	0.307
st26gm07n001	1.0	0.315	6953	281^3	1381	∞	27.74	400	2635	-0.77	1.416	0.256
st28gm06n26	1.0	0.182	6955	281^3	1381	∞	25.35	371	2737	-0.70	1.290	0.317
st29gm06n001	1.0	0.109	6948	281^3	1381	∞	25.35	348	2822	-0.65	1.150	0.314
st27gm06n001	1.0	0.548	4982	281^3	1381	∞	28.53	345	2610	-0.64	1.230	0.088
st28gm05n002	1.0	0.262	4978	281^3	1381	∞	25.35	313	2742	-0.56	1.077	0.104
st28gm05n001	1.0	0.182	4990	281^3	1381	∞	25.36	300	2798	-0.52	1.026	0.135
st29gm04n001	1.0	0.141	4982	281^3	1381	∞	25.35	294	2827	-0.50	0.927	0.100

The table shows the model name (composed of the approximate effective temperature and surface gravity and of a running number), the mass $M_\star$ used for the external potential, the envelope mass $M_{\rm env}$ (all the mass actually contained in the computational box), the average emitted luminosity $L_\star$ (close but not identical to the inserted luminosity of either 5000, 7000, or 10000 $L_\odot$ in the core), the model dimensions $n_x \times n_y \times n_z$, the edge length of the cubical computational box $x_{\rm box}$, the rotational period $P_{\rm rot}$, the time used for the averaging of the rest of the quantities $t_{\rm avg}$, the average approximate stellar radius $R_\star$, the average approximate effective temperature $T_{\rm eff}$, the logarithm of the average approximate surface gravity $\log g$, the pulsation period $P_{\rm puls}$, and the half width of the distribution of the pulsation frequencies $\sigma_{\rm puls}$. The first ("old") group comprises models used in Freytag & Höfner (2008). In the second ("test") group, numerical parameters (e.g., the box size or the number of grid points) or the rotation period were varied. The last ("grid") group comprises models with slightly varying stellar parameters ($M_{\rm env}$, $L_\star$).

CO5BOLD solves the coupled non-linear equations of compressible hydrodynamics (with an approximate Roe solver) and non-local radiative energy transfer (for global models with a short-characteristics scheme) in the presence of an external gravitational field. The numerical grid is Cartesian. In all models presented here, the computational domain as well as all individual grid cells are cubical. The tabulated equation of state takes into account the ionization of hydrogen and helium and the formation of H_2 molecules. It is assumed that solar abundances are appropriate for M-type AGB stars. The tabulated grey opacities (very similar to the ones used in Freytag & Höfner 2008) are merged from Phoenix (Hauschildt et al. 1997) and OPAL (Iglesias et al. 1992) data at around 12 000 K, with a slight reduction in the very cool layers (that are hardly reached in the current model grid) to remove any influence of dust onto the opacities. There are no source terms or dedicated opacities for dust: no dust is included in any of the current models, in contrast to the two old models st28gm06n05 and n06.

The gravitational potential is spherically symmetric, corresponding to 1 $M_\odot$ in the outer layers and smoothed in the center at $r \lesssim R_0 = 78\,R_\odot$ (see Fig. 4 in Freytag & Höfner 2008). The tiny central nuclear-reaction region cannot possibly be resolved with grid cells of constant size. Instead, in the smoothed-core region, a source term feeds in energy corresponding to 5000, 7000, or 10000 $L_\odot$. A drag force is active only in this core to prevent dipolar flows traversing the entire star. All outer boundaries are open for the flow of matter and for radiation.

Table 1 and Fig. 1 give an overview over the simulations, split into three groups: old models from Freytag & Höfner (2008), new test models used for parameter studies (including rotation rate), and a grid of models with different stellar parameters.

While for instance the mass $M_\star$ (controlling the gravitational potential), the resolution and the extent of the numerical grid, and the rotation rate are pre-chosen fixed parameters (2nd group of rows in Table 1), others are determined after a simulation is finished (3rd group in Table 1): the stated stellar luminosity is a time average of the luminosity for each "fine" snapshot (with lots of pre-processed data, saved every 250 000 s ≈ 3 d), while the envelope mass $M_{\rm env}$ is calculated from the integrated density for each snapshot, averaged over time. However, the radius is more difficult to determine and less well defined. It is chosen as that point $R_\star$ where the spherically (abbreviated as $\langle . \rangle_\Omega$) and temporally (denoted as $\langle . \rangle_t$) averaged temperature and the average luminosity $\langle L \rangle_{\Omega,t}$ fulfill $\langle L \rangle_{\Omega,t} = 4\pi\sigma R_\star^2 \langle T \rangle_{\Omega,t}^4$. Then, effective temperature and surface gravity follow.

To investigate purely radial motions we take averages over spherical shells for each snapshot for the radial mass flux $\langle \rho v_{\rm radial} \rangle_\Omega(r,t)$ and the mass density $\langle \rho \rangle_\Omega(r,t)$ and take the ratio as the radial velocity, which is now a function $\langle v_{\rm radial} \rangle(r,t)$ of radial distance and time. The derivation of $P_{\rm puls}$ and $\sigma_{\rm puls}$ is described in Sect. 3.3.

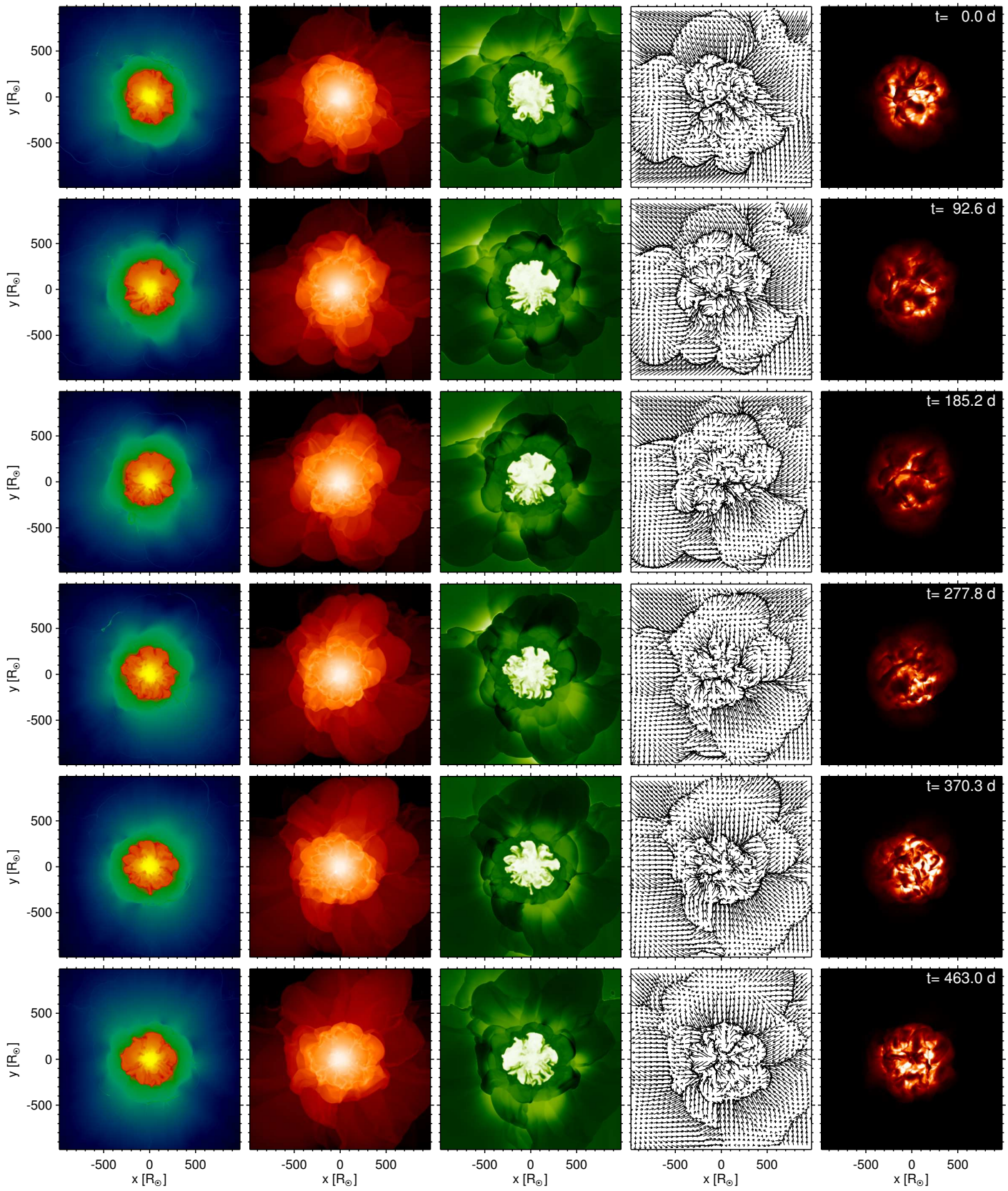

Fig. 2. Time sequences (for the extended model st28gm06n25) of temperature slices, density slices, entropy slices, pseudo streamlines (integrated over about 3 months), and bolometric intensity maps. The snapshots are nearly 3 months apart (see the counter in the right-most panels), so that the entire sequence covers about one pulsational cycle. The figure can be directly compared to Fig. 1 of Freytag & Höfner (2008).

3. Results

3.1. General dynamics and comparison to old models

The time evolution of various quantities can be followed in the snapshot sequences in Figs. 2 and 3 and the plots of radial velocity as function of radius and time in Fig. 4 (in a certain stencil: $v_{\rm radial}(r,t)$) and Fig. 5 (averaged over spheres: $\langle v_{\rm radial}\rangle_\Omega(r,t)$).

3.2. Convective motions

The convection zone is essentially marked by the bright (high entropy) irregular inner part of the entropy snapshots in Fig. 2 with a radius around $300\,R_\odot$, which is smaller than the inferred stellar radius of $R_\star = 371\,R_\odot$ given in Table 1, i.e., light is emitted from layers further out. The drop in entropy at the top of the convective layers is accompanied by a drop in temperature and even a thin density-inversion layer.

Huge convective cells can span 90 degrees or more in the cross sections, in line with extrapolations by Schwarzschild (1975) from solar granulation. The cells are outlined by non-stationary downdrafts reaching from the surface of the convection zone to the center of the model star. While the flow-travel time from the surface to the center is around half a year, the convective cells can have a lifetime of many years, causing long intervals of one preferred flow direction in the convection zone in Fig. 4. These downdrafts even have a tendency to traverse the artificial stellar core and to create a global dipolar flow field. However, in the (non-rotating) models presented here, the drag force – somewhat deliberately – applied in the stellar core prevents these flows.

The surface of the convection zone appears corrugated, caused by many smaller short-lived "granulation" cells close to the surface. Their number increases with numerical resolution, as a comparison of Fig. 2 with Fig. 1 of Freytag & Höfner (2008) reveals.

Simulations of red supergiants (RSGs) with CO5BOLD (Freytag et al. 2002; Chiavassa et al. 2009; Arroyo-Torres et al. 2015) show large-scale convection cells, too, but for RSGs the ratio of surface pressure scale height – and therefore the size of the convective structures and the local radius fluctuations – to radius is smaller than for AGB stars, so that RSGs appear more spherical.

3.3. Pulsations

3.3.1. Exploring the pulsation mode and period

The density snapshots in Fig. 2 show irregular structures, with convection cells in the interior and a network of shocks in the atmosphere. To investigate purely radial motions we consider the density-weighted spherical average of the radial velocity $\langle v_{\rm radial}\rangle(r,t)$ as described in Sect. 2 and plotted in Fig. 5 for the standard model st28gm06n26.

The behavior of the inner part of the model differs from that of the atmosphere, particularly evident in Fig. 5. Below about $400\,R_\odot$ (the nominal radius is $R_\star = 371\,R_\odot$), the pulsation is rather regular and coherent over all layers, close to a standing wave. The fundamental mode is dominating, as there are no nodes in the velocity map, In the outer layers, however, the slopes in the velocity map indicate propagating shock waves (see Sect. 3.4).

In the right panel in Fig. 5, a close-up of part of the velocity field is shown, with movements of mass shells as overlay, analogous to plots for the 1D models, for example in Höfner et al. (2003) or Nowotny et al. (2010). The amplitude of the 3D mass-shell oscillations is smaller than for corresponding 1D models by a factor of two or more. This is – at least partly – due the averaging over the full 3D model, which smoothes the amplitude as the shock waves are not exactly spherical.

To quantify the periodic behavior a Fourier analysis is performed using the averaged radial velocity $\langle v_{\rm radial}\rangle(r,t)$. An example for $r = 301\,R_\odot$ is shown in the left panel of Fig. 6, again for model st28gm06n26, with the corresponding power spectrum in the right panel. Frequencies around $0.6\,{\rm yr}^{-1}$ dominate.

To explore the behavior all through the star the power spectra of the averaged radial velocity $\langle v_{\rm radial}\rangle(r,t)$ at all radii are plotted in the middle panel of Fig. 7. Again the two different behaviors in the inner and outer layers of the model are evident. There is a dominant frequency in the stellar interior, as suspected from Fig. 5. However, the outer layers beyond $r \sim 400\,R_\odot$ no longer pulsate with the same period as the interior of the star. Lower-frequency signals become more prominent and beyond $r \sim 600\,R_\odot$ (far out in the shock-dominated atmosphere) the frequency with the largest amplitude is significantly smaller than that of the interior of the star.

In the power spectra of models with different stellar parameters in Fig. 7, the dominant mode generally becomes more diffuse with increasing radius of the model. For more compact models, for instance model st29gm04n001 with $R_\star = 294\,R_\odot$ in the left panel in Fig. 7, there is a very clear dominant mode in the interior. For the standard model (middle panel in Fig. 7 with radius $R_\star = 371\,R_\odot$) there is still a dominant frequency, but the spread around this frequency is larger. For the largest model (model st28gm07n001 with $R_\star = 531\,R_\odot$ in the right panel in Fig. 7), the power spectrum seems to be equally distributed over a large frequency range, lacking a clear dominant frequency which is present in the two other models.

To find the dominant frequency and therefore the pulsation period, as well as to investigate the spread in frequencies, the area-normalized power spectra of the radial velocities for radial distances $r = 0.5 - 1\,R_\star$ were added. For instance, this corresponds to radial points in the range $r = 185.5 - 371\,R_\odot$ for the standard model. A Gaussian distribution was fitted in the frequency domain containing the strongest signal. The central value for the fit for each model is taken as the dominant frequency $f_{\rm dom}$, while the spread in frequencies is represented by the standard deviation $\sigma_{\rm puls}$. The resulting periods $P_{\rm puls} = 1/f_{\rm dom}$ and spreads $\sigma_{\rm puls}$ are listed in Table 1 and plotted in Fig. 9 where the colors of the squares represent the temperature, with lighter colors indicating higher temperature, and the size represents the luminosity of the model, as seen in Fig. 1.

3.3.2. Excitation mechanism

The irregular spread of the mode frequencies in Fig. 7, is likely due to interactions between the pulsations and large-scale convective motions causing occasional amplitude changes and phase shifts. With larger radius, the convective cells increase further in relative size resulting in stronger disturbances of the pulsation mode. Within a luminosity group the frequency spread grows with decreasing radius, which is likely due to the increase of convective velocities with increasing effective temperature, cf. the bottom-right panel in Fig. 10.

Analyzing light curves, Christensen-Dalsgaard et al. (2001) attributed oscillations in semiregular variables to stochastic excitation by convection. Bedding et al. (2005) distinguished several cases: they attributed large phase fluctuations in the light curve of the semiregular star W Cyg to stochastic excitation, whereas

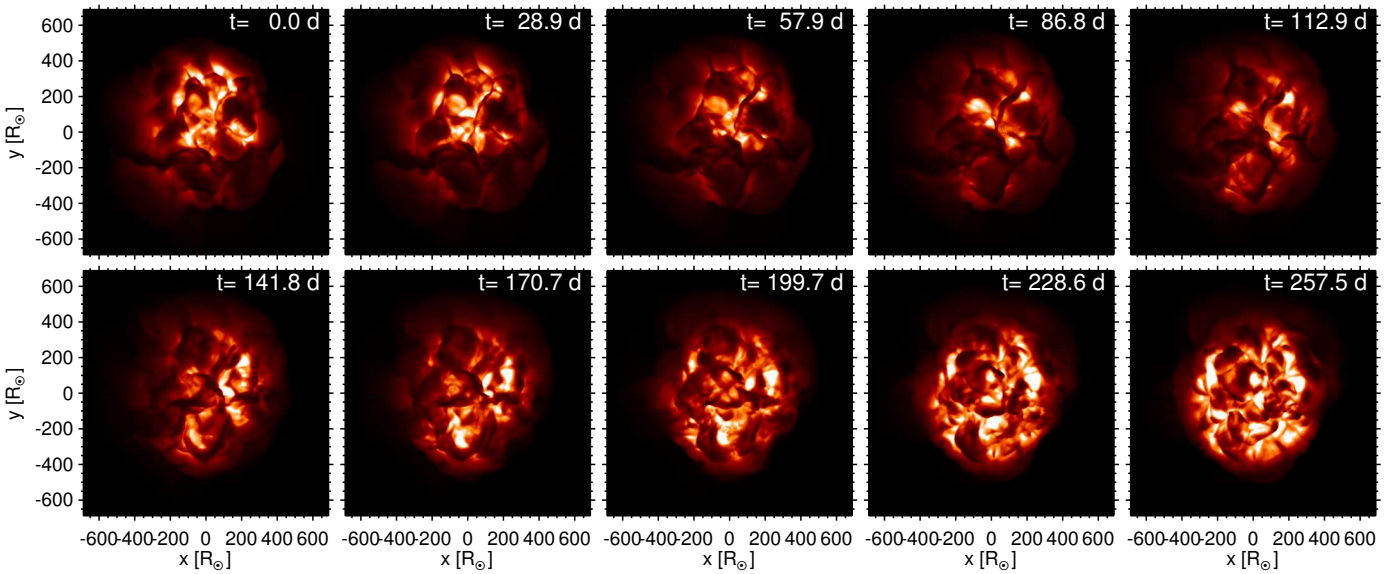

Fig. 3. Time sequence (for the standard model st28gm06n26) of bolometric intensity maps. The snapshots are about 1 month apart to demonstrate the relative short time scale for changes of the small surface features.

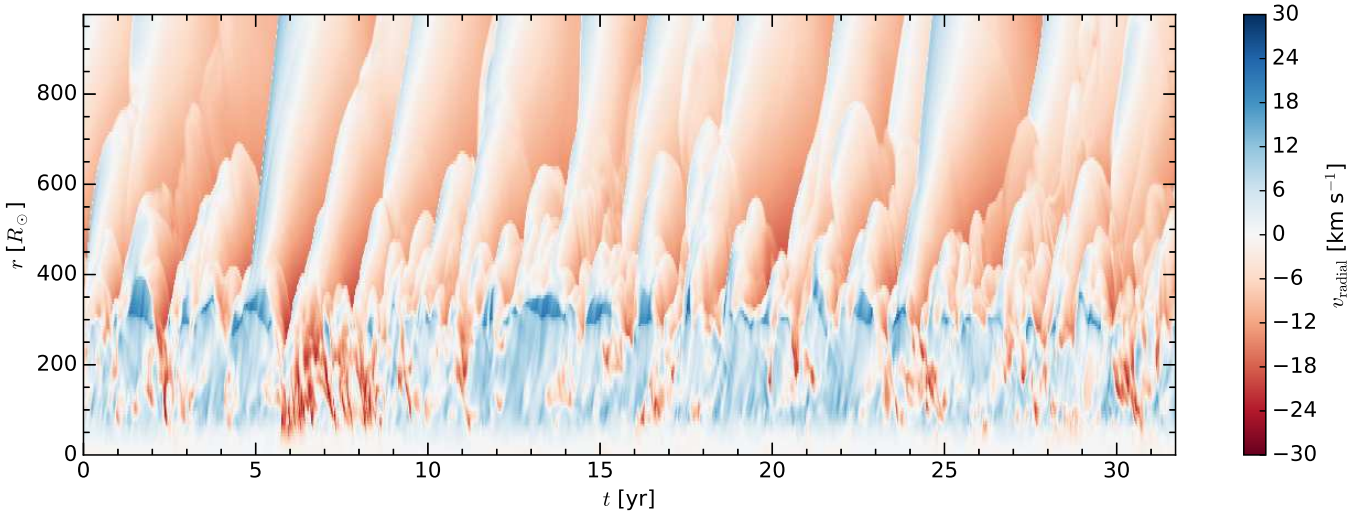

Fig. 4. Plot (for the standard model st28gm06n26) of radial velocity $v_{\rm radial}(r,t)$ for all grid points in one column from the center to the side of the computational box for the entire simulation time. Blue indicates outward and red inward flow.

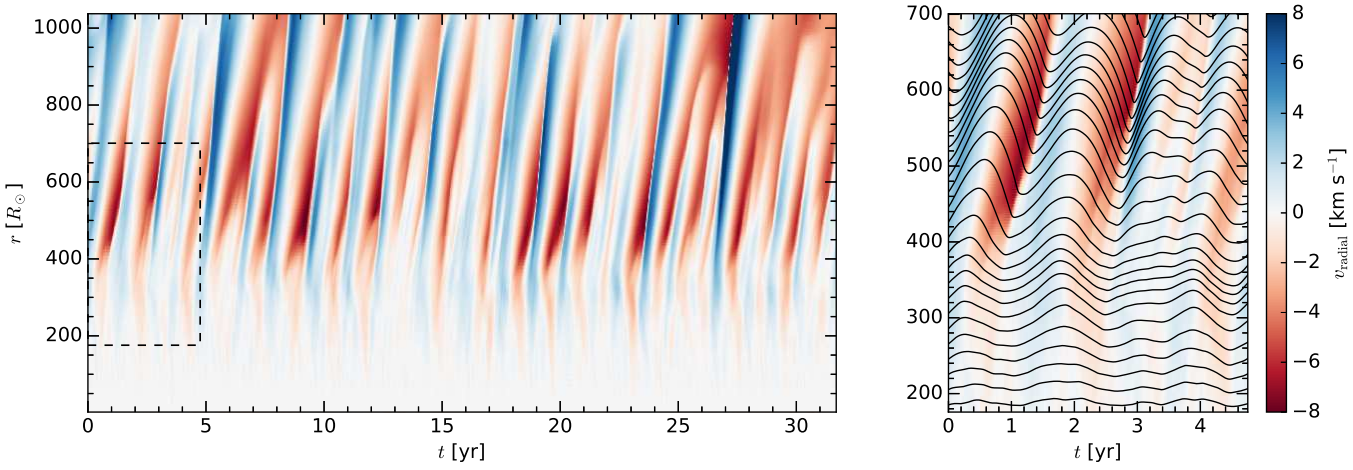

Fig. 5. For the standard model st28gm06n26; *Left* – The radial velocity $\langle v_{\rm radial}\rangle_\Omega(r,t)$ for the full run time and radial distance. The different colors show the average vertical velocity at that time and radial distance. *Right* – Part of the velocity field from the right image, marked with the rectangle, with mass-shell movements plotted as iso-mass contour lines.

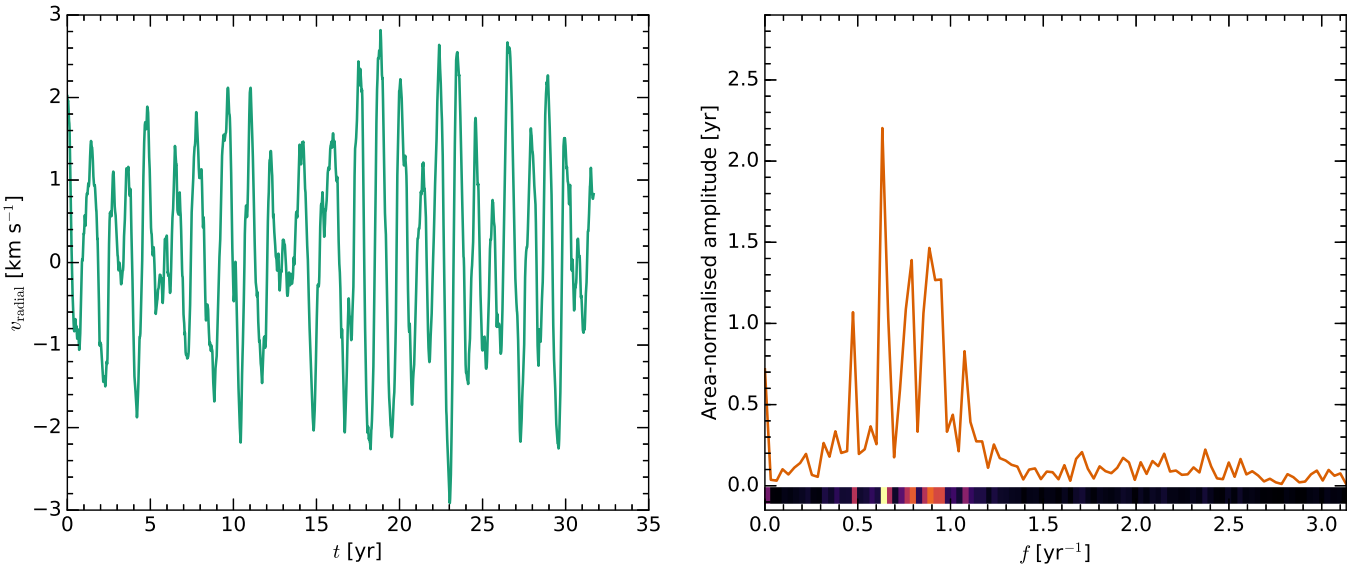

Fig. 6. For the standard model st28gm06n26; *Left* – The vertical velocity at a constant $r = 301\,R_\odot$, over 30 years. *Right* – The power spectrum of the vertical velocity, shown to the left, showing the clearly dominant frequency. At the bottom of the panel, the density plot for this power spectrum is shown. This type of data is used in Fig. 7 for all radial points.

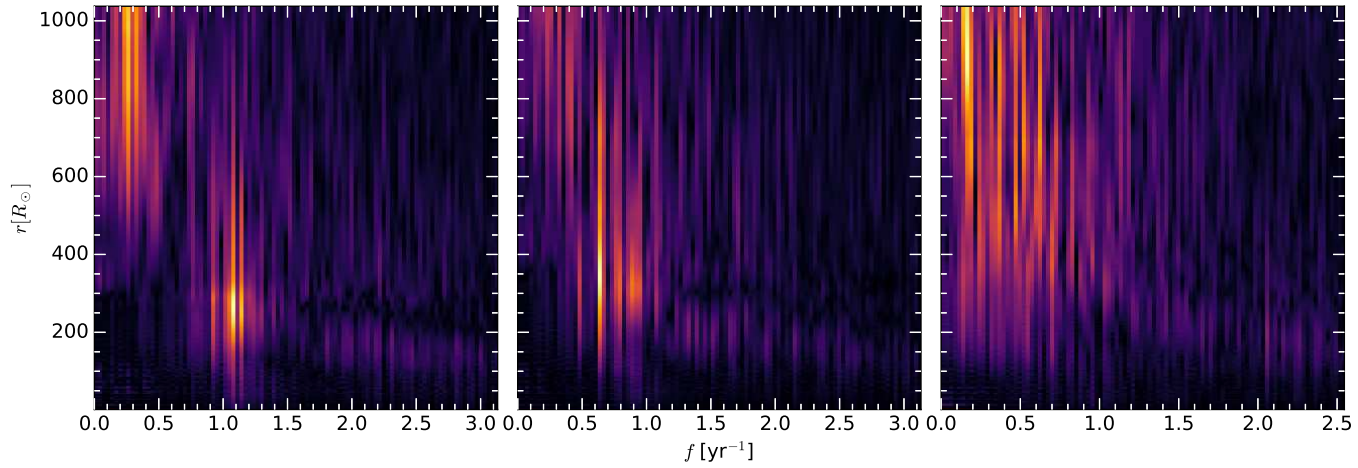

Fig. 7. Power spectra derived from the velocity fields of three different models, mapped over frequency and radial distance. For easier comparison all the different power spectra have been area normalized. *Left* – Model st29gm04n001, the hottest and smallest model. *Middle* – The standard model st28gm06n26. *Right* – Model st28gm07n001, the coolest and most luminous model, with the largest radius.

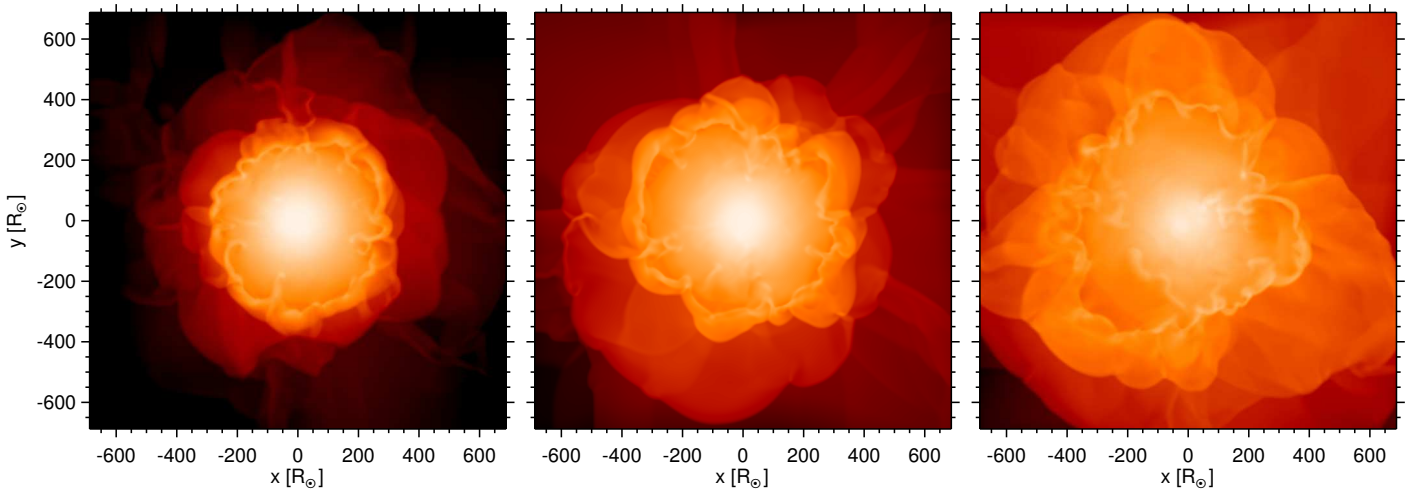

Fig. 8. Density slices for the three models used in Fig. 7. The range used for all color tables is $-16 \leq \log \rho \leq -6.7$.

the very stable phase of the true Mira star X Cam was found to consistent with the excitation by the κ mechanism. L_2 Pup was classified as intermediate case where both mechanisms play a role.

Analyzing the work integral in 1D pulsation models Lattanzio & Wood (2004) concluded that the driving mechanism at least for Mira variables is likely a κ mechanism acting in the partial hydrogen and helium I ionization zone.

Our grid of 3D models, that by far does not cover the entire range of AGB stars, already shows a range of different behaviors of the oscillations (see Fig. 7 and the discussion in the previous section), where the trend clearly points at the role of convection and the size of the convective cells for the excitation of – or at least interaction with – the pulsation. The non-stationary transsonic convective flows with Mach numbers in the downdrafts often exceeding unity produce acoustic noise as described by Lighthill (1952) for turbulent flows. This excitation mechanism has been investigated for instance by Nordlund & Stein (2001) and Stein & Nordlund (2001) with local 3D radiation-hydrodynamics simulations of solar granulation. The Mach numbers in near-surface convective flows of AGB stars can be even larger causing more efficient wave excitation (Lighthill 1952). As the relative sizes of the exciting convective structures are very large, the generated waves have much lower wave numbers than on the Sun.

To check that the radial pulsations are not just (long-lasting) transient phenomena introduced by the initial conditions, we added a strong (purely artificial) drag force in the entire model volume. It reduced the amplitude of the pulsations (and the convective flows) but did not lead to an exponential decay of the radial mode, indicating that an efficient mode-excitation mechanism has to be at work.

In the models of Freytag & Höfner (2008), these pulsations existed and their amplitude was extracted as description for the piston boundary in 1D models. However, the global pulsations were harder to distinguish from the local shock network because of the lower numerical resolution, that lead to larger sizes of convective and wave structures, and the shorter time sequences, that made a Fourier analysis less reliable than what is possible for the current model grid.

3.3.3. Comparison with 1D models and observations

As has been pointed out by Fox & Wood (1982) and Wood (1990), AGB stars do not seem to follow the simple period-mean-density relationship, $P_{\rm puls} \times (\bar{\rho}/\bar{\rho}_\odot)^{1/2} = Q$, where Q is the pulsation constant. This is not very surprising as the derivation of the period-mean-density relationship relies on the assumptions that displacements are adiabatic and non-linear effects are small, both probably incorrect for AGB stars. Instead these works, using 1D pulsation models, find that $P_{\rm puls} \propto R_\star^\alpha M_\star^{-\beta}$, with $\alpha \sim 1.5$ – 2 and $\beta \sim 0.5 - 1$. The period-radius relationship for our models with a fixed mass $M_\star = 1\,M_\odot$ is compared to that of Fox & Wood (1982) and Wood (1990) in the left panel of Fig. 9. We find

$$\log(P_{\rm puls}) = 1.39\,\log(R_\star) - 0.9\ , \qquad (1)$$

which gives generally a larger radius for a given period. There might be several reasons for this difference (in addition to uncertainties in the 1D models):

There is a contribution to the extension of the atmosphere of the 3D models (see Sect. 4.2) due to the convectively-generated small-scale shocks (see Sect. 3.4), that does not exist in the 1D models. This would affect the radius but not the pulsation period if the thin atmosphere just sits on top of the pulsating cavity. And it might even lower the slope, because the largest models have the most extended atmospheres. The convective envelope is not in hydrostatic equilibrium but affected by the convective dynamical pressure, too. In addition, the treatment of the artificial core in the 3D models might play a role. However, the effect should be small because the sound-crossing time for the core – and therefore the contribution to the period – is relatively small. Finally, we there is some uncertainty in the determination of radius and period.

In the left panel of Fig. 9, observations of the radii for different AGB stars are plotted against the periods, with C stars as crosses and M stars as circles. The diameter observations are from Richichi et al. (2005), the periods from Samus et al. (2009), and the parallaxes from van Leeuwen (2007). The 3D models agree fairly well with observations, especially the lower-luminosity models. The period-radius relationship from the 1D models might produce too long periods for the range of radii explored by the 3D models when compared to observations. It is however difficult to draw final conclusions as the uncertainty of radius observations are very large, sometimes of the order of the stellar radius, and different observational methods tend to give different result.

A quantity that is better constrained by observation is the P-L relationship, which has been extensively studied. A comparison between the 3D models and observation by Whitelock et al. (2009) is shown in the right panel of Fig. 9. The models from the grid follow a trend of brighter absolute magnitude with larger period, which is qualitatively similar to that of the observations. There is however a spread in the periods, due to the different effective temperatures and radii for a given luminosity, giving constraints for our – so far a bit arbitrary – choice of the combination of the main control parameters $M_\star$, $M_{\rm env}$, $L_\star$, and metallicity of the 3D models.

3.4. Atmosphere with a network of shocks

The steepening of acoustic waves in the solar chromosphere, and the transformation into a network of shocks was modelled by Wedemeyer et al. (2004). AGB stars have a larger temperature drop from the convection zone to the atmosphere (cf. Figs. 5 and 6 in Freytag & Chiavassa 2013, for a model sequence from the Sun to a 5 $M_\odot$ star), accompanied by a larger change in pressure or density scale height. This leads to a stronger compression and amplification of the waves in the cool atmosphere, so that the waves very early turn into shocks leaving no room for an essentially undisturbed photosphere. Sound-speed variations particularly at the rugged surface of the convection zone and transsonic convective flow speeds shape the waves and contribute to the appearance of small-scale shock structures (at $r > 300\,R_\odot$ in Fig. 4), that give rise to ballistic curves with peak heights of a few ten to a few hundred solar radii. The strongest shocks can even leave the computational box.

The plot of entropy vs. radius in Fig. 10 shows that part of the atmosphere has a zone of convective instability – with negative entropy gradient – separate from the normal interior convection zone. The image sequences in Fig. 2 and the plot of $v_{\rm radial}(r,t)$ in Fig. 4 show a very different behavior in both zones: only the inner one is governed by the "normal" overturning motions, whereas propagating shocks dominate in the outer one (as discussed in Sect. 3.3.1). But still, the convective instability might destabilize the shocks favoring a tendency towards smaller structures as seen in the intensity snapshots in Figs. 2 and 3. For models with $L = 5000\,L_\odot$, this instability zone lies "further out"

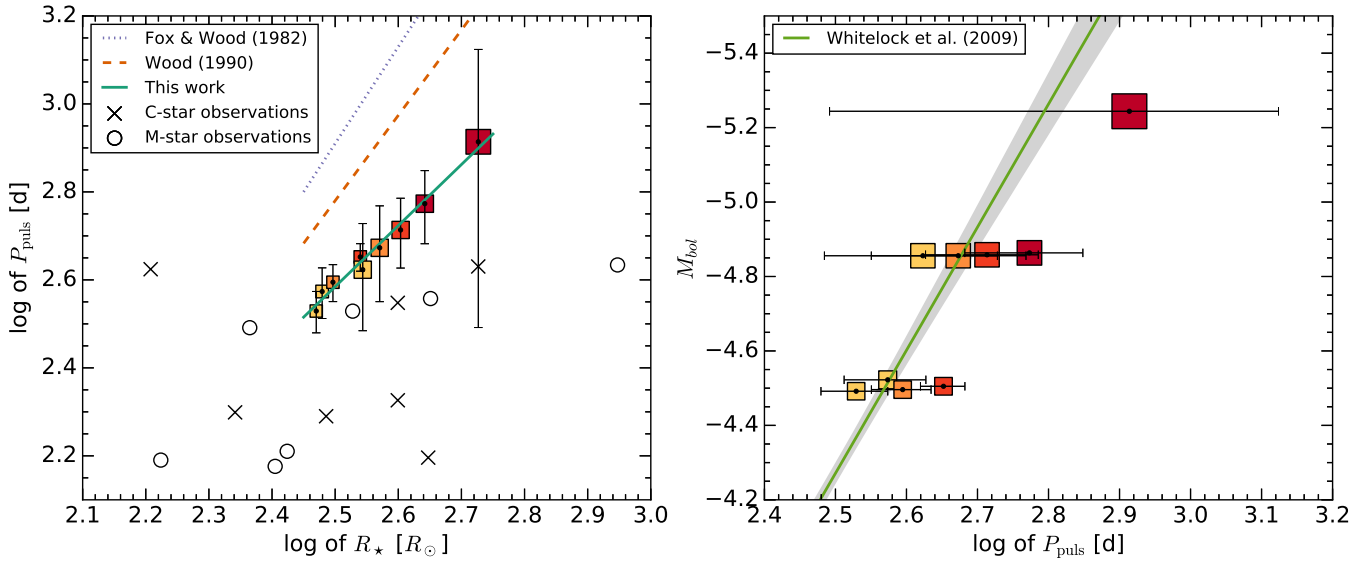

Fig. 9. *Left* – The logarithm of the period of the models plotted against the logarithm of the resulting radius, with three different period-radius relationship plotted; green is from this work, orange is from Wood (1990), and purple is from Fox & Wood (1982). The crosses and circles are observations of C stars and M stars respectively, with radius from the CHARM2 catalog (Richichi et al. 2005) and periods from GCVS catalog (Samus et al. 2009). Only stars with measured parallaxes where picked, so that the distance determination is independent of the measured period (Ramstedt & Olofsson 2014). *Right* – The absolute magnitude against the logarithm of the period for all models. The line is taken from Whitelock et al. (2009) and is the P-L relationship for AGB stars in the LMC, with the grey area being the 1 σ error of the fit to the observations.

relative to the stellar radius compared to the higher-luminosity models. Woitke (2006) showed that in 2D simulations of the atmosphere of an AGB star, where the radial stellar pulsation and inhomogeneities generated by convection are ignored and shocks are generated by an external κ mechanism, instabilities *within* the shock fronts can cause small-scale structures to form.

A combination of relatively small-scale acoustic noise and global, radial pulsations generates the network of shocks, with a size spectrum regulated by a number of complex processes: a wave emitted from a small region close to the surface might turn into an expanding shock wave, that fills a large part of the atmosphere if the surrounding flow permits it. The overtaking and merging of shocks increases the typical size. On the other hand are large-scale waves in the interior shaped by the background flow and sound-speed distribution and can become as rugged as the surface of the convection zone itself. And the convective instability in the atmosphere favors small scales, too.

The shock fronts show up prominently in the density slices in Fig. 2 and are only occasionally visible in the temperature slices (e.g., in the upper left quadrant in the fourth row) because the radiative relaxation is – even with the used grey opacity table – fast enough to cool down the heated post-shock material to the local equilibrium value. The radiative relaxation time further decreases when non-grey opacity tables are employed (in a currently running first simulation), essentially wiping out any temperature signature of the shocks. That might change again with a drastic increase in numerical resolution, that is currently not achievable.

While the temperature stratifications of the various models in Fig. 10 show lots of differences in the convection zone and inner atmosphere, they converge into one of three profiles in the outer atmosphere, depending only on stellar luminosity. This and the relatively small temperature fluctuations in the outer part of the temperature slices in Fig. 2 indicate that the outer atmosphere is not far from radiative equilibrium. The shocks show up in the velocities and the density but hardly in the temperature.

Expectedly, the size spectrum of the shocks is extended towards finer scales with increasing resolution as a comparison of Fig. 2 of the current paper with Fig. 1 of Freytag & Höfner (2008) demonstrates.

3.5. Rotation

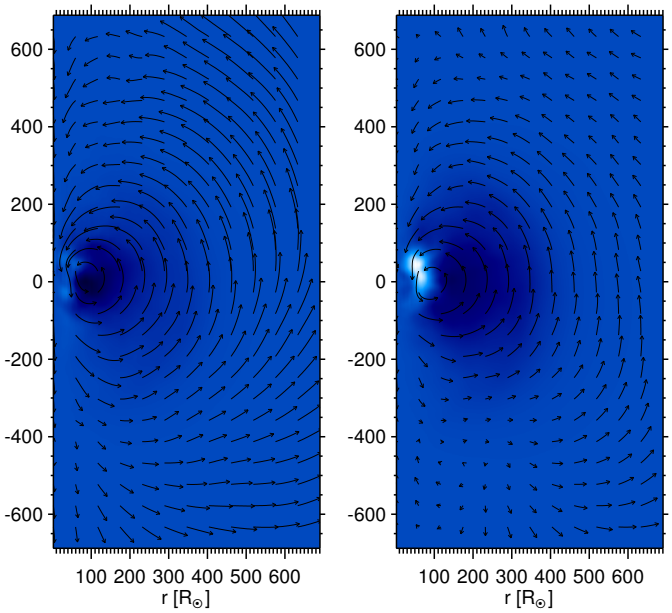

Fig. 11. Azimuthally and temporally averaged velocity fields for model st28gm06n29 ($P_{\rm rot}$ = 20 yr, left) and st28gm06n30 ($P_{\rm rot}$ = 10 yr, right). The color plot shows the angular momentum in the co-rotating frame (bright-blue means rotation faster than the mean, dark-blue means rotation slower than the mean).

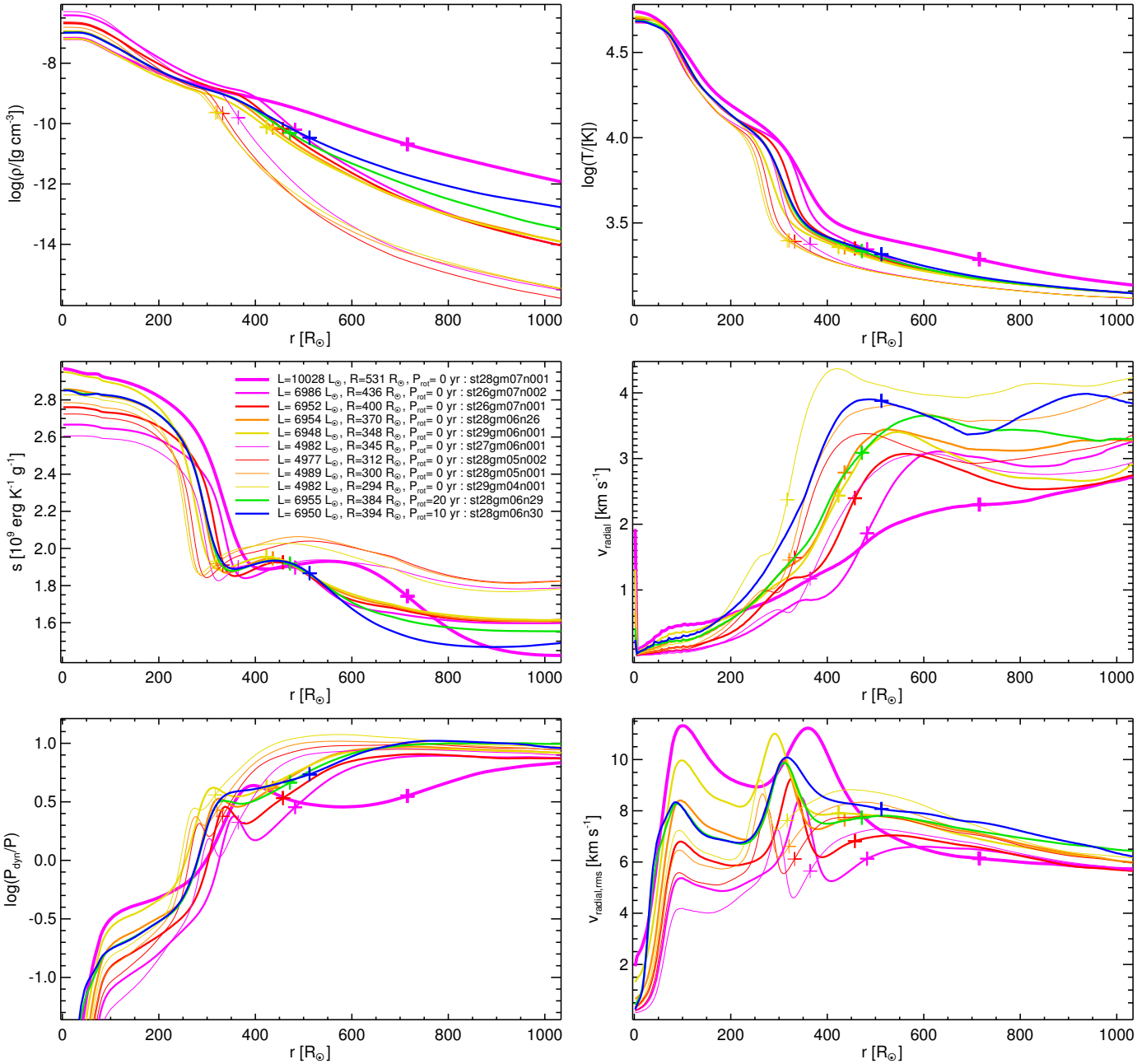

Fig. 10. Plot of selected quantities, averaged over spherical shells and time, versus radius for all grid models. The plus signs roughly indicate the depth with $\tau_{\rm Ross} = 1$. *Top left* – Logarithm of the mass density ρ. *Top Right* – Logarithm of the temperature T. *Center left* – Entropy per mass unit s. *Center right* – Temporal rms value of the spherically averaged radial velocity (includes mostly contributions from the radial pulsations). *Bottom left* – Logarithm of the ratio of dynamical pressure $P_{\rm dyn}$ and gas pressure P. *Bottom right* – Temporal and spatial rms value of the radial velocity (includes contributions both from convection and radial pulsations).

Rotation plays an important role for stellar activity and possibly also for stellar winds. The loss of angular momentum due to magnetic coupling with the surroundings or due to wind will likely slow down evolved stars considerably. Dorfi & Höfner (1996) performed 1D models of the stationary wind of a 1 $M_\odot$/2600 K/10000 $L_\odot$ AGB star and find that a rotation period of 40 yr modifies the isotropic mass loss marginally, while a period of 10 yr results in a drastic increase of the mass loss rate and causes a significant axial asymmetry of the wind.

Hydrodynamical simulations of convection and rotation have been performed of the solar interior or stellar interiors, where the Mach numbers are low, so that the flow is essentially incompressible, and the opacities are so high, that radiation transport is adequately described by the diffusion approximation.

However, these conditions are not met in the convective envelopes and surrounding atmospheres of AGB stars, where the numerical treatment in CO5BOLD (e.g., of non-local radiation transport and compressible hydrodynamics) is adequate, so we modified the CO5BOLD setup to account for rotation. While it is possible to just add a rotational velocity field to the initial model, we chose to perform the simulation in a co-rotating frame. A centrifugal potential is added to the gravitational potential. Before each hydrodynamics step the Coriolis force is applied, which just rotates the velocity vectors, but with twice the

amount simply suggested by period and time step. The artificial drag force in the model core was chosen to act only radially to not affect the angular momentum. We computed a first exploratory pair of models with rotation periods of 20 and 10 years (see Table 1). Longer periods would require even longer integration times. The $P = 20$ yr simulation was started from a snapshot from a non-rotating run and the period (i.e., centrifugal potential and Coriolis force) were increased gradually over a few stellar years to avoid transient oscillations due to a too rapid change of the potential.

As expected for slow rotators, where the rotational period is longer than typical convective turnover time scales, angular momentum is advected inward into a small region close to the core of the model (see Fig. 11). In spite of the drag force in the core, a global dipole flow develops with typical velocities in the atmosphere of $v_{\rm meridional}$=4 km/s (for st28gm06n29 with $P_{\rm rot} = 20$ yr) and $v_{\rm meridional}$=2.5 km/s (for st28gm06n30 with $P_{\rm rot} = 10$ yr).

While the core generally rotates very rapidly, the part of the convection zone that is not close to the axis rotates slower than the nominal rate. Part of the material close to the core of the model with $P_{\rm rot} = 20$ yr even shows a slow retrograde rotation. However, all azimuthally averaged velocity components show large fluctuations and the averaging time or the relaxation time for this model might not yet be sufficient.

The mean atmospheric stratification is affected by the rotating star: while the temperature stratification shows hardly any effect, the average density in the atmosphere increases with shorter rotation period (see Fig. 10).

Our rotating models have a number of shortcomings: The approximation of the smoothed stellar core plays are larger role than for not rotating purely convective (and pulsating) flows. Would the angular momentum in a real star be advected even further in and leave only a very slowly rotating convective envelope and atmosphere behind? What role would magnetic fields play in coupling the interior to the convective envelope? The outer boundaries might influence the results, too, because the slowly rotating atmosphere moves with respect to the computational box and might exchange angular momentum through the boundaries. Clearly, improved models need a larger computational domain and and update of the treatment of the stellar core.

Still, the presented models confirm the results of Dorfi & Höfner (1996) that rotation in AGB stars – if the period is of the order of 20 yr or shorter – can influence the atmospheric velocity field and the wind and might be responsible for the shapes of some planetary nebulae.

4. Discussion

4.1. Influence of numerical parameters

The current models have an improved resolution over the ones presented in Freytag & Höfner (2008) due to an increased number of grid points and a higher-order reconstruction scheme of the hydrodynamics solver (Freytag 2013). While sub-surface convection cells and above-surface shocks show finer structures, there are no qualitative changes in the general results. Still, the newer models allow a better separation of the radial mode from the convective noise and present a longer time base for the Fourier analysis.

The averaged density stratifications for selected models in Fig. 12 give an idea about the size of effects due to changes in numerical parameters. The two smallest (and oldest) models n02 and n06 (referring to the last three letters of the model names) used already in Freytag & Höfner (2008) have the same resolution but different extensions and agree well with each other. The same is true for the pair n24/n25 from the current "test" group of models, indicating that the box size does not have a major impact. The curves for n24 and n26 (our standard model) just lie on top of each other. The difference is a change in code version, accompanied mainly by a modification of the WENO scheme used for the high-order reconstruction in the hydrodynamics solver. The numerical resolution was increased in model n16 compared to n13 with only a slight effect onto the mean-density stratification.

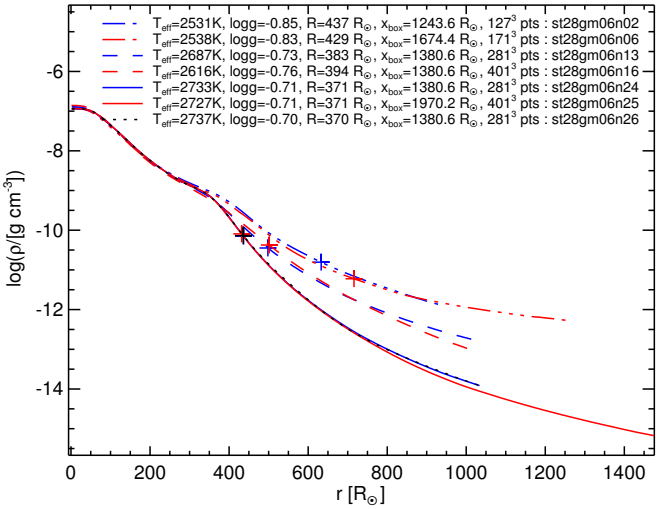

Fig. 12. Logarithm of the gas density averaged over spherical shells and time for six models. The ordering in the legend essentially corresponds to the order of the curves. The plus signs roughly indicate the depth with $\tau_{\rm Ross} = 1$. In the legend, the effective temperature, surface gravity, edge length of the computational box, number of grid points, and the name are given for each model.

The noticeable decrease of the density by about one order of magnitude in the outer layers from n13/n16 to n24/n25/n26 is caused by a change in the outer boundary conditions: assuming a less steep density decrease outside the boundaries induces a stronger infall of material in the phase between outward moving shocks and somewhat impedes the shocks, leading to lower averaged densities in the outer layers. An additional reduction might be due to a difference in the treatment of the velocity damping in the core region of the models. Omitting such a damping, large-scale dipolar flows could develop and dominate the entire convective envelope. Between the old models n02/n06 and the new ones, there are differences in the envelope mass $M_{\rm env}$ and too many changes in the numerics to allow a disentanglement of the influence of individual settings.

4.2. Dynamical pressure

The bottom-left panel in Fig. 10 shows the time-averaged ratio of the radial component of the dynamical pressure averaged over spheres and the averaged gas pressure $\langle\langle\rho v^2_{\rm radial}\rangle_\Omega/\langle P\rangle_\Omega\rangle_t$. In addition, the rms value of the radial velocities $\langle v^2_{\rm radial}\rangle^{1/2}_{\Omega,t}$, that are responsible for the dynamical pressure, and the (smaller) contribution by the radial pulsations $\langle(\langle\rho v_{\rm radial}\rangle_\Omega/\langle\rho\rangle_\Omega)^2\rangle^{1/2}_t$ are plotted in the bottom-right and the middle-right panels, respectively.

Already in the convection zone, where the pressure ratio is below one, it stays above 20 % for a number of models for quite a fraction of the radius. Thus, the dynamical pressure is not neg-

ligibly small and might have an influence on the stratification at least of the outer convective envelope. The peak of the radial velocities near the surface of the convection zone is accompanied by a peak in the pressure ratio, and the dynamical pressure becomes even larger than the gas pressure.

Further out in the atmosphere, the dynamical pressure dominates over the gas pressure (radiation pressure is not included in the current models) by factor 5 to 10. It significantly increases the density and pressure scale heights compared to hydrostatic values causing a levitation of dense material into cool layers. This allows molecules to appear and possibly creates a highly irregular, non-spherical, and dynamic version of a "MOLsphere" (Tsuji 2000). And the conditions become even sufficient for dust to form (see e.g., Freytag & Höfner 2008). The contributions of the purely radially symmetric motions (middle-right panel in Fig. 10) and of the spatially fluctuating flows to the total radial velocities (bottom-right panel in Fig. 10) are both significant. Only the first type can be accounted for by dynamical 1D models, though.

While we get very extended atmospheres in our models of *AGB stars*, Arroyo-Torres et al. (2015), concluded that for *red supergiant stars* (with much larger masses) the dynamical pressure in 1D models and the – considerable – dynamical pressure in 3D-CO5BOLD models is not sufficient to sufficiently enlarge the photosphere to bring it close to observed huge extensions.

4.3. Fine structures in the atmosphere

Some observations (e.g., by VLT/SPHERE, HST, VLTI and various other interferometers, or with the Cassini spacecraft) of asymmetries and clumps in the dust envelopes of near-by AGB stars have been presented in the Introduction.

The bolometric-intensity maps in Figs. 2 and 3 derived from the 3D models show that the smallest scale patterns change on time scales of less than a month, while intensity changes of larger areas occur on time scales of a about a year.

The surface of the "normal" stellar convection zone (see Sect. 3.2) sits too deep to directly affect the emergent intensity: we don't see surface granules or larger convection cells themselves. Instead, the visible structures are caused by shocks on various scales. However, as described in Sect. 3.4, the shocks are shaped by the underlying convective structures. A dimming and brightening of a large area (see Fig. 3) might well indirectly reflect the dynamics of the convection.

A detailed comparison of results from the 3D models with observations has to await simulations with non-grey opacities and a detailed treatment of dust.

4.4. Characteristic time scales

A comparison of the pulsation period with the various typical time scales of convective structures (see Sect. 3.2) gives

$$t_{\rm granule} \ll t_{\rm downdraft} \sim \frac{1}{2}\, t_{\rm turnover} \lesssim P_{\rm puls} \ll t_{\rm giant-cell} \ , \qquad (2)$$

i.e., that the granules adjust to the pulsation whereas the giant cells are more or less frozen in. However, a restructuring of the giant cells can lead to a variation of the detailed pulsation behavior on rather long time scales, of several years. The strongest interaction is to be expected between pulsations and downdrafts. There is no such thing as "the" convective time scale.

5. Conclusions

We presented a first exploratory grid of 3D radiation-hydrodynamics models of AGB stars computed with a new version of CO5BOLD, improved in terms of accuracy, stability, and boundary treatment over the simulations presented in Freytag & Höfner (2008). The increased effective resolution leads to additional finer structures in the convective flow (surface granules and deep turbulent eddies) and near-surface shocks. However, there is no significant change in the dynamical behavior of the models and only a small one in spatially (over spheres) and temporally averaged quantities.

Several interacting processes govern the dynamics of the atmosphere of the model AGB stars: non-stationary convection manifests as *giant convective cells* that change topology on very long time scales – outlined by turbulent downdrafts, that reach from the surface of the convection zone down into the very core of the model – and short-lived *small surface granules*. Convective motions emit *acoustic waves* ("noise", comparable to solar p modes) and shape – i.e., distort – wave fronts. In addition, there are *large-amplitude, radial, fundamental-mode pulsations*. The small-scale acoustic waves steepen when they reach the thin cool atmosphere and turn into shocks. The shocks interact and merge, so that the scale of the atmospheric shocks increases with radial distance, from a *fine shock network* close to the surface of the convection zone, to distorted but *almost global, more or less radially expanding shock fronts* in the outer layers. The cycles of outward moving shocks and material falling back towards the star have a longer period than the pulsations themselves.

The radial pulsations have realistic properties in spite of the complete neglect of the details of the real stellar core in the models. The models reproduce the correct period for a given luminosity, compared to observation, if we chose an appropriate ratio of envelope mass to luminosity. The radius of the 3D models is however larger for a given period, compared to previously found period-radius relationships from 1D pulsation models. The reason for this is not clear as it could be a physical explanation for the larger radius, based on 3D dynamical processes, or it could be due to shortcomings of the 1D models. Higher-gravity models have a clearly defined pulsation period, whereas the lower-gravity objects show a much more irregular behavior, depending on the relative size of the convection cells and the typical convective flow speed.

The convective cells themselves do not reach out into visible layers. However, the network of shocks propagating (into a partially convectively unstable) atmosphere gives rises to short-lived spatial inhomogeneities across the stellar "disk", that might be the cause for observed dynamical features.

Inside the convection zone, the dynamical pressure is smaller than the gas pressure but still not negligible and has to be accounted for in detailed stellar-structure models. However, in the atmosphere, the dynamical pressure exceeds the gas pressure (by a factor of up to 10). Both global shocks induced by radial pulsations as well as small-scale shocks (that are not accounted for in 1D models) contribute to the levitation of material that can give rise to a "MOLsphere" and that allows dust to form.

Comparison of the properties of the pulsation found in the 3D models with those from 1D models and observations give confidence that the 3D models provide a reliably qualitative description of the outer convection zone and the inner part of the atmosphere of AGB stars. However, further work is needed (e.g., the use of non-grey opacity tables, a grid with a larger range of stellar parameters, a larger computational box, and a description

of dust) to make the 3D models ready for a more detailed quantitative confrontation with observations.

Acknowledgements. The computations were performed on resources ("milou") provided by SNIC through Uppsala Multidisciplinary Center for Advanced Computational Science (UPPMAX) under Project p2013234.

References

Arroyo-Torres, B., Wittkowski, M., Chiavassa, A., et al. 2015, A&A, 575, A50
Bedding, T. R., Kiss, L. L., Kjeldsen, H., et al. 2005, MNRAS, 361, 1375
Beeck, B., Cameron, R. H., Reiners, A., & Schüssler, M. 2013, A&A, 558, A48
Bladh, S., Höfner, S., Aringer, B., & Eriksson, K. 2015, A&A, 575, A105
Bowen, G. H. 1988, ApJ, 329, 299
Chandler, A. A., Tatebe, K., Wishnow, E. H., Hale, D. D. S., & Townes, C. H. 2007, ApJ, 670, 1347
Chiavassa, A., Plez, B., Josselin, E., & Freytag, B. 2009, A&A, 506, 1351
Christensen-Dalsgaard, J., Kjeldsen, H., & Mattei, J. A. 2001, ApJ, 562, L141
Dorfi, E. A. & Höfner, S. 1996, A&A, 313, 605
Eriksson, K., Nowotny, W., Höfner, S., Aringer, B., & Wachter, A. 2014, A&A, 566, A95
Fleischer, A. J., Gauger, A., & Sedlmayr, E. 1992, A&A, 266, 321
Fox, M. W. & Wood, P. R. 1982, ApJ, 259, 198
Freytag, B. 2013, Mem. Soc. Astron. Italiana Suppl., 24, 26
Freytag, B. & Chiavassa, A. 2013, in EAS Publications Series, Vol. 60, EAS Publications Series, ed. P. Kervella, T. Le Bertre, & G. Perrin, 137–144
Freytag, B. & Höfner, S. 2008, A&A, 483, 571
Freytag, B., Steffen, M., & Dorch, B. 2002, Astronomische Nachrichten, 323, 213
Freytag, B., Steffen, M., Ludwig, H.-G., et al. 2012, J.Comp.Phys., 231, 919
Haniff, C. A. & Buscher, D. F. 1998, A&A, 334, L5
Hauschildt, P. H., Baron, E., & Allard, F. 1997, ApJ, 483, 390
Höfner, S. 2008, A&A, 491, L1
Höfner, S. 2015, in Astronomical Society of the Pacific Conference Series, Vol. 497, Why Galaxies Care about AGB Stars III: A Closer Look in Space and Time, ed. F. Kerschbaum, R. F. Wing, & J. Hron, 333
Höfner, S., Gautschy-Loidl, R., Aringer, B., & Jørgensen, U. G. 2003, A&A, 399, 589
Iglesias, C. A., Rogers, F. J., & Wilson, B. G. 1992, ApJ, 397, 717
Ireland, M. J., Scholz, M., & Wood, P. R. 2008, MNRAS, 391, 1994
Ireland, M. J., Scholz, M., & Wood, P. R. 2011, MNRAS, 418, 114
Jeong, K. S., Winters, J. M., Le Bertre, T., & Sedlmayr, E. 2003, A&A, 407, 191
Karovska, M., Hack, W., Raymond, J., & Guinan, E. 1997, ApJ, 482, L175
Karovska, M., Nisenson, P., Papaliolios, C., & Boyle, R. P. 1991, ApJ, 374, L51
Kastner, J. H. & Weintraub, D. A. 1994, ApJ, 434, 719
Lattanzio, J. C. & Wood, P. 2004, in "Asymptotic Giant Branch Stars", eds. Habing H.J., Olofsson H., Springer, 23–104
Lighthill, M. J. 1952, Royal Society of London Proceedings Series A, 211, 564
Lopez, B., Danchi, W. C., Bester, M., et al. 1997, ApJ, 488, 807
Ludwig, H.-G., Caffau, E., Steffen, M., et al. 2009, Mem. Soc. Astron. Italiana, 80, 711
Magic, Z., Collet, R., Asplund, M., et al. 2013, A&A, 557, A26
Nordlund, Å. & Stein, R. F. 2001, ApJ, 546, 576
Nowotny, W., Höfner, S., & Aringer, B. 2010, A&A, 514, A35
Ohnaka, K., Weigelt, G., & Hofmann, K.-H. 2016, A&A, 589, A91
Ramstedt, S., Mohamed, S., Vlemmings, W. H. T., et al. 2014, A&A, 570, L14
Ramstedt, S. & Olofsson, H. 2014, A&A, 566, A145
Richichi, A., Percheron, I., & Khristoforova, M. 2005, A&A, 431, 773
Samus, N. N., Durlevich, O. V., & et al. 2009, VizieR Online Data Catalog, 1
Schwarzschild, M. 1975, ApJ, 195, 137
Stein, R. F. & Nordlund, Å. 2001, ApJ, 546, 585
Stewart, P. N., Tuthill, P. G., Monnier, J. D., et al. 2016a, MNRAS, 455, 3102
Stewart, P. N., Tuthill, P. G., Nicholson, P. D., & Hedman, M. M. 2016b, MNRAS, 457, 1410
Stothers, R. & Leung, K.-C. 1971, A&A, 10, 290
Tremblay, P.-E., Ludwig, H.-G., Freytag, B., et al. 2015, ApJ, 799, 142
Tsuji, T. 2000, ApJ, 540, L99
van Leeuwen, F. 2007, A&A, 474, 653
Wedemeyer, S., Freytag, B., Steffen, M., Ludwig, H.-G., & Holweger, H. 2004, A&A, 414, 1121
Weigelt, G., Balega, Y., Blöcker, T., et al. 1998, A&A, 333, L51
Whitelock, P. A., Feast, M. W., & van Leeuwen, F. 2008, MNRAS, 386, 313
Whitelock, P. A., Menzies, J. W., Feast, M. W., et al. 2009, MNRAS, 394, 795
Winters, J. M., Le Bertre, T., Jeong, K. S., Helling, C., & Sedlmayr, E. 2000, A&A, 361, 641
Woitke, P. 2006, A&A, 452, 537
Wood, P. R. 1990, in From Miras to Planetary Nebulae: Which Path for Stellar Evolution?, ed. M. O. Mennessier & A. Omont, 67–84
Wood, P. R., Alcock, C., Allsman, R. A., et al. 1999, in IAU Symposium, Vol. 191, Asymptotic Giant Branch Stars, ed. T. Le Bertre, A. Lebre, & C. Waelkens, 151